

# Inter-mosaic coordination of retinal receptive fields

<https://doi.org/10.1038/s41586-021-03317-5>

Suva Roy<sup>1</sup>, Na Young Jun<sup>1</sup>, Emily L. Davis<sup>1</sup>, John Pearson<sup>1,2</sup> & Greg D. Field<sup>1,✉</sup>

Received: 15 July 2020

Accepted: 1 February 2021

Published online: 10 March 2021

 Check for updates

The output of the retina is organized into many detector grids, called ‘mosaics’, that signal different features of visual scenes to the brain<sup>1–4</sup>. Each mosaic comprises a single type of retinal ganglion cell (RGC), whose receptive fields tile visual space. Many mosaics arise as pairs, signalling increments (ON) and decrements (OFF), respectively, of a particular visual feature<sup>5</sup>. Here we use a model of efficient coding<sup>6</sup> to determine how such mosaic pairs should be arranged to optimize the encoding of natural scenes. We find that information is maximized when these mosaic pairs are anti-aligned, meaning that the distances between the receptive field centres across mosaics are greater than expected by chance. We tested this prediction across multiple receptive field mosaics acquired using large-scale measurements of the light responses of rat and primate RGCs. ON and OFF RGC pairs with similar feature selectivity had anti-aligned receptive field mosaics, consistent with this prediction. ON and OFF RGC types that encode distinct features have independent mosaics. These results extend efficient coding theory beyond individual cells to predict how populations of diverse types of RGC are spatially arranged.

Mosaics are a fundamental organizing feature of retinal output<sup>2,7</sup>. This output is formed by RGCs, which transmit signals to the brain along their axons. Most, if not all, types of RGC form mosaics, meaning that the receptive fields (RFs) of each type are regularly spaced and approximately tile the retina. This produces a complete, uniform and efficient encoding of visual scenes<sup>1–3,6,8</sup>. Furthermore, many types of RGC come in functionally similar pairs, with one member signalling increments of a particular visual feature and the other signalling decrements. These functionally related pairs also serve to efficiently encode visual stimuli<sup>9,10</sup>, and frequently form ‘pathways’ through the brain that converge downstream; for example, ON and OFF parasol RGCs in primates form the magnocellular pathway and ultimately converge in primary visual cortex<sup>5</sup>. The convergence of ON and OFF signals strongly shapes cortical processing and possibly perception<sup>11–14</sup>. This organization of visual signalling raises the question of how the mosaics of different types of RGC should be arranged to efficiently encode natural scenes. Answering this question is important because visual processing ultimately depends not on the activity of a single cell or cell type, but on the activity of large populations of diverse cell types.

There are many ways in which two mosaics can be spatially arranged, but we focus on three broad categories: independent, aligned and anti-aligned. For a pair of independent mosaics, the locations of RFs in one mosaic provide no information about RF locations in the other mosaic. This organization is commonly assumed on the basis of anatomical measurements of retinal cell bodies<sup>15–17</sup>, but cell body locations only weakly constrain RF locations<sup>17</sup>. For aligned mosaics, the locations of RFs across mosaics would tend to be closer than expected by chance. Finally, for anti-aligned mosaics, the centres of RFs across mosaics would tend to be farther apart than expected by chance. Each arrangement has potential advantages. Alignment puts two detector grids in spatial registration, potentially facilitating the encoding or decoding of

stimuli, whereas anti-alignment might provide higher spatial resolution or make the system more robust to noise<sup>18</sup>. Independence may strike a balance between these two states, or simply be straightforward to achieve developmentally.

## Efficient coding predicts anti-alignment

We began by examining the predictions of a simple model of retinal processing that is optimized according to efficient coding theory (ECT)<sup>6</sup>. The model consists of an ensemble of linear filters (representing RFs) and rectifying nonlinearities (representing the transformation from filtered visual input to spike rates). Input and output noise are included to model noise in phototransduction and spike generation, respectively. Finally, the model includes a cost function for generating spikes (Fig. 1a). We optimized the linear filters and nonlinearities to maximize the mutual information between a library of 10,000 natural images and simulated spike counts of the model retina. Consistent with previous results<sup>6</sup>, the optimized model converged on centre–surround RFs organized into two mosaics: a mosaic of ON RFs and a mosaic of OFF RFs (Fig. 1b–d). This division of ON and OFF RFs reduces the spiking output of the system<sup>6,9</sup>. Other than the polarity difference, the RFs and nonlinearities were similar across the two mosaics, indicating that these mosaics mimic a pair of cell types that encode similar visual features, but with opposite polarities.

We next analysed the relative spatial arrangements of RFs across the pair of optimized mosaics to determine whether they were independent, aligned or anti-aligned. To distinguish among these possibilities, each RF was reduced to its centre-of-mass (COM), thus reducing the mosaics to two grids of points (Fig. 1e). We quantified the relative spacing between points across the two mosaics by the sum over the squared inverse distances between all pairs of heterotypic points, which was

<sup>1</sup>Department of Neurobiology, Duke University, Durham, NC, USA. <sup>2</sup>Department of Biostatistics and Bioinformatics, Duke University, Durham, NC, USA. <sup>✉</sup>e-mail: field@neuro.duke.edu

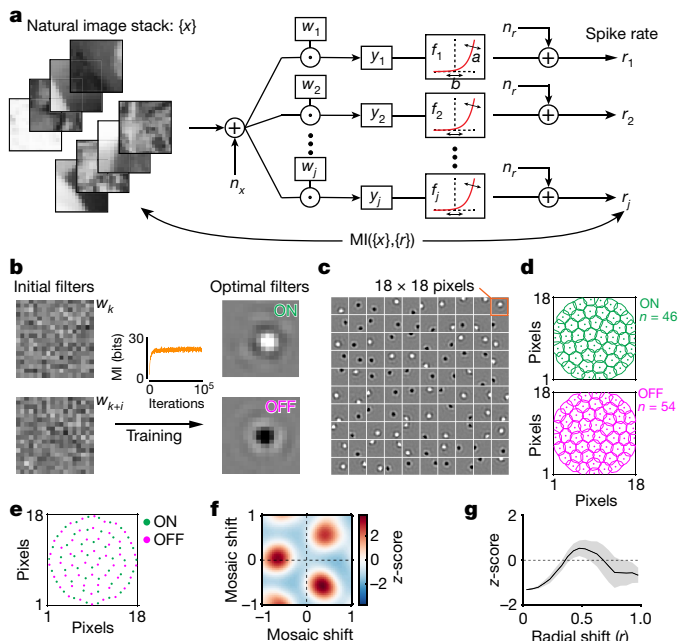


**Fig. 1 | Efficient coding predicts anti-alignment between ON and OFF RGCs with similar feature selectivity.** **a**, The schematized model was trained on about 10,000 natural images to maximize the mutual information (MI) between input and the collection of responses ( $r_1, r_2, \dots, r_j$ ) under noise and metabolic constraints (see Methods).  $x$ , input images;  $n_x$ , input noise;  $w$ , linear filter;  $y$ , filtered output;  $f$ , nonlinear function;  $n_r$ , output noise. **b**, Noisy spatial filters ( $w$ ) at the beginning of training (left) become centre-surround filters by end of training (right). The two learned filters exemplify ON (positive contrast) and OFF (negative contrast) RFs. Middle inset, change in MI with training. **c**, All 100 filters after optimization. Each square patch is  $18 \times 18$  pixels (orange box). **d**, The COMs (filled circles) and 1 s.d. contours around the COMs (outlines) for  $n = 46$  ON-centre (green) and  $n = 54$  OFF-centre (magenta) filters on the  $18 \times 18$ -pixel grid. These define the ON and OFF mosaics. **e**, Centre points of all ON-centre and OFF-centre model neurons. **f, g**, Two-dimensional z-scored IMCE map (**f**) and z-scored radial average IMCE (**g**) for the ON and OFF mosaic pairs in **e** show that the mosaics generated from the efficient coding model are anti-aligned (Fig. 2). Shaded area, s.d.

restricted to a maximum value for points closer than a distance  $r_{\min}$  (see Methods). This distilled the inter-mosaic relationship down to a single number, which we call the inter-mosaic coordination energy (IMCE). The IMCE is motivated by the idea of a potential energy function that weights local interactions more strongly than distal interactions<sup>11</sup>.

We then rigidly shifted one mosaic with respect to the other and recomputed the IMCE for each  $\Delta x$  and  $\Delta y$  shift (Fig. 2e), to compare the observed arrangement with alternative arrangements at different shifts. The IMCEs across all shifts were then z-scored (normalized by the standard deviation of observed IMCEs). The distribution of IMCEs approximately followed a normal distribution, confirmed by kurtosis, skewness and percentile measurements (Extended Data Table 1).

To gain insight into coordination from the IMCE, we used a modified pairwise interaction point-process (PIPP) model<sup>19–21</sup> to generate two sets of points (types 1 and 2) with specific homotypic and heterotypic interactions (see Methods). This allowed homotypic pairs of points to maintain a regular spacing observed in mosaics, while generating mosaic pairs that were anti-aligned (Fig. 2a), aligned (Fig. 2b), or spatially independent (Fig. 2c). If two mosaics are anti-aligned (Fig. 2a), the IMCE tends to increase as one mosaic is rigidly shifted with respect to the other, yielding a lower IMCE for arrangements (Fig. 2f). The radial average of the two-dimensional IMCE map yields a function that has a trough near zero (Fig. 2i). Conversely, if two mosaics are aligned, the IMCE tends to decrease as a function of shift distance (Fig. 2b, g, j).

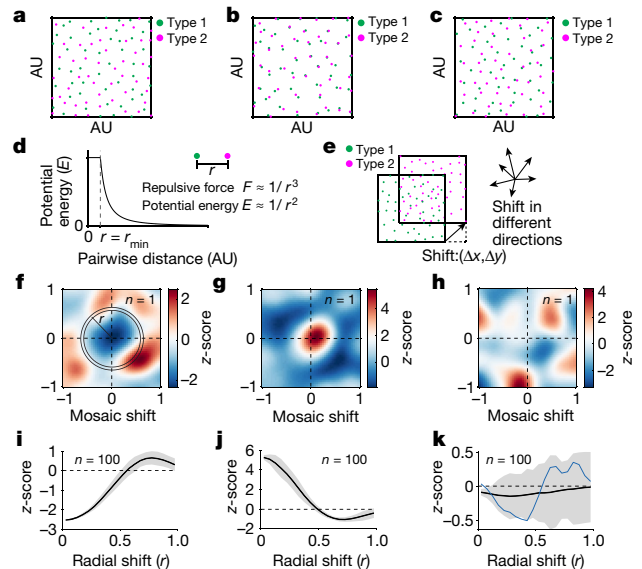


**Fig. 2 | Analysis framework for measuring mosaic coordination.** **a–c**, Pairs of ON (green) and OFF (magenta) mosaics generated from a modified PIPP model with specific constraints on homotypic (ON–ON, OFF–OFF) and heterotypic (ON–OFF) interactions (see Methods) exhibit anti-alignment (**a**), alignment (**b**) and independence (**c**). Each point represents the COM of the spatial RF.  $x$ -axis and  $y$ -axis units are arbitrary (AU). Each ON and OFF mosaic contains 50 points. **d**, The repulsive energy between two points as a function of their separation  $r$ . The energy is set to a constant value for  $r \leq r_{\min}$  (see equation (3)). Inset, inverse cube repulsive force,  $F$ , and potential energy,  $E$ , between two heterotypic points (green and magenta). **e**, ON mosaic (green) rigidly shifted with respect to OFF mosaic (magenta), by different amounts and along different directions (length and direction of arrow, respectively), for estimating 2D IMCE map. **f–h**, 2D z-scored IMCE maps for anti-aligned (**f**), aligned (**g**) and independent (**h**) mosaic pairs ( $n = 1$ ).  $x$ - and  $y$ -axes have units of normalized shift. The z-scored IMCE is averaged over an annulus (shown in **f**) at different radial distances to obtain the radial z-scored IMCE curve. **i–k**, Average over  $n = 100$  radial z-scored IMCE curves, each obtained by radially averaging the 2D z-scored IMCE map for anti-aligned (**i**), aligned (**j**) and independent (**k**) mosaic pairs. The radial z-scored IMCE curve for the 2D z-scored IMCE map in **h** is shown in blue (**k**). Shaded area, s.e.m.

For independent mosaics (Fig. 2c), the IMCE map does not exhibit a consistent topographical structure (Fig. 2h), and hence the radial average is relatively flat as a function of shift distance (Fig. 2k). Note, we use this ‘energy’ analysis only to examine coordination between mosaics; we do not postulate that an actual energy exists between mosaics or was involved in their development.

Applying this analysis to the ON and OFF mosaics optimized according to ECT indicated that they were anti-aligned (Fig. 1e–g). We confirmed the robustness of this result by (1) training the model on a set of independently collected natural images (see Methods); (2) using more- or less-severe cost functions on spiking; (3) changing the number of filters; and (4) forcing the number of filters with ON and OFF centres to be unequal (Extended Data Fig. 1), including very different cell densities in the simulated mosaics (Extended Data Fig. 2). The optimized mosaics from the efficient coding model remained anti-aligned under these manipulations.

## ON and OFF RGC mosaics are anti-aligned

Following these predictions from ECT, we tested whether measured RGC mosaics exhibited this predicted spatial organization. To measure the spatial relationships across RGC mosaics, we used a large-scale multi-electrode array (MEA) to map the RF locations of diverse types of RGC<sup>22,23</sup>. We presented a spatiotemporal white noise stimulus to ex

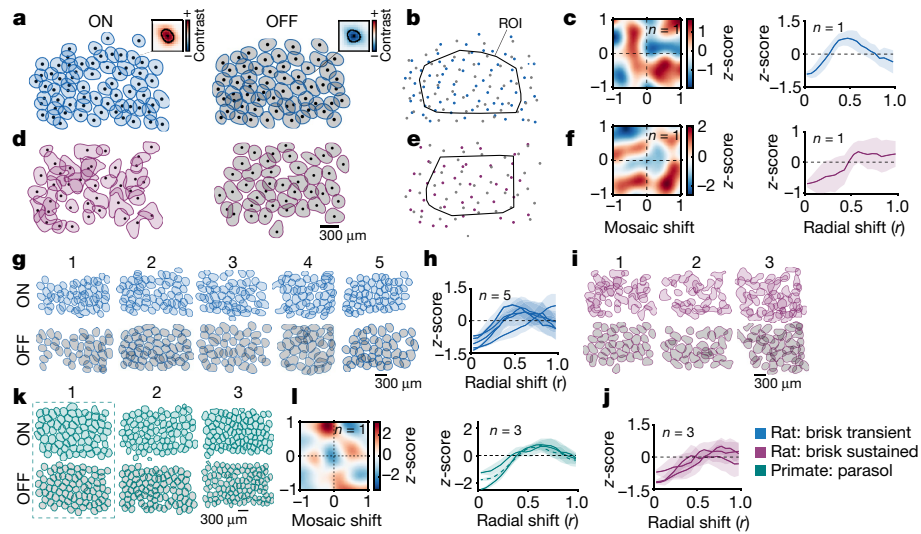


**Fig. 3 | Receptive field mosaics of functionally paired ON and OFF RGC types are anti-aligned.** **a**, Representative ON (left, light blue shaded) and OFF (right, grey shaded) RF mosaics of brisk transient RGCs from rat (blue). RF contours are at 61% of peak ( $-1\text{s.d.}$  for a Gaussian RF). Black dots show COMs. Insets, spatial RFs of individual RGCs with contours and COMs. **b**, The COMs of RFs of all ON (blue) and OFF (grey) brisk transient RGCs. Black contour, region of interest (ROI) used in analysis (see Methods). **c**, Left, 2D z-scored IMCE map as a function of shift between ON and OFF brisk transient mosaics (**a**). Mosaic shift normalized to the mean homotypic nearest-neighbour distance. Right, radial average z-scored IMCE. **d–f**, As in **a–c** but for ON and OFF brisk sustained

RGCs (magenta). **g**, RF mosaics of ON and OFF brisk transient RGCs from five retinas; each column shows one retina. **h**, Radial average z-scored IMCE as a function of mosaic shift for five mosaic pairs shown in **g**. **i, j**, As in **g, h** for three pairs of ON and OFF brisk sustained RGCs, each from a different retina. **k**, RF mosaics of ON (top) and OFF (bottom) parasol RGCs from three primate retinas (green). **l**, Left, 2D z-scored IMCE map of a representative primate retina (dashed box in **k**). Right, radial average z-scored IMCE for the three primate retinas as a function of mosaic shift. Dashed curve corresponds to the 2D z-scored IMCE map on the left. Shaded areas, s.d.

vivo rat retina and calculated the spike-triggered average stimulus for each RGC to estimate its spatial and temporal RF<sup>24</sup>. A typical experiment yielded spikes from about 300–400 RGCs that were functionally classified according to their spatiotemporal RFs and other response properties (see Methods)<sup>23,25</sup>. RF locations were not used in the classification (see Methods), but the RFs of each clustered RGC type exhibited a mosaic-like arrangement (Fig. 3a, d), which confirms that the types of RGC are functionally distinct and irreducible<sup>1,23,26,27</sup>.

We focused on four types of RGC for which we frequently measured nearly complete mosaics (Fig. 3a, d, g, i). These four types comprised two pairs of ON and OFF cells that were otherwise functionally similar: brisk transient and brisk sustained RGCs<sup>23</sup>. Thus, they were analogous to the pair of types generated by the efficient coding model (Fig. 1) and allowed us to examine the relationships between multiple pairs of real RGC mosaics that encode either similar (up to a polarity flip) or distinct visual features.

First, we examined ON and OFF brisk transient RGCs, which encode temporally bandpass stimuli and exhibit strongly rectified contrast responses<sup>23</sup>. The IMCE maps were less periodic than those generated from ECT (Fig. 1) because the biological mosaics were more disordered. Nevertheless, the IMCE between these RGC mosaics rose with shift distance (Fig. 3b, c), indicating that they were anti-aligned. Next, we examined ON and OFF brisk sustained RGCs, which exhibit relatively low-pass temporal filtering and more linear contrast responses. These mosaics also exhibited an IMCE that rose with shift distance (Fig. 3e, f), indicating anti-alignment. These results were consistent across multiple mosaics measured from different rat retinas (Fig. 3g–j). Thus, ON and OFF RGC types that form functional pairs exhibit anti-aligned mosaics, consistent with predictions from ECT (Fig. 1f, g).

If anti-alignment between ON and OFF RGC mosaics is driven by the efficient encoding of natural scenes, it should persist in other terrestrial species. Thus, we examined the spatial relationships between mosaics of ON and OFF parasol cells in the primate retina<sup>28</sup>. An analysis of IMCE also revealed anti-alignment between these functionally similar (but

opposite polarity) RGC types (Fig. 3k, l). Thus, anti-alignment of ON and OFF mosaics generalizes across RGC types in at least two species.

To test the robustness of these results to mosaic imperfections, such as gaps caused by missing RFs, we examined the extent to which artificially adding or removing RFs from measured mosaics altered these results (Extended Data Fig. 3a). The radial dependence of the IMCE was robust up to a reduction of about 20% in the number of RFs in the mosaic (Extended Data Fig. 3b, c). Artificially adding RFs to ‘gaps’ in the measured mosaics reduced variability in the IMCE estimates but did not alter the qualitative results for mosaic anti-alignment observed in rat or primate retinas (Extended Data Fig. 3b, c).

We next assessed the likelihood that the observed anti-alignment between mosaics occurred by chance. We constructed a null distribution for mosaic coordination by combining ON and OFF RGC mosaics measured from different rat and primate retinas. These ‘pseudo-pairs’ of mosaics are statistically independent, and therefore should yield radial IMCE curves distinct from those of aligned or anti-aligned mosaics. We spatially registered each pseudo-pair of mosaics based on their COM (see Methods). The distribution of IMCE across pseudo-pairs remained largely unaltered for small offsets between the COMs. To quantify anti-alignment, we calculated the weighted area under the radial IMCE profile curve (see Methods) for both real and pseudo-pairs (Fig. 4a). The real pairs exhibited values that were outside the confidence bounds of the null distribution generated from the pseudo-pairs (Fig. 4b, c, Extended Data Table 2), indicating a low probability that the observed anti-alignment in the measured mosaics arose by chance.

## Mosaics are independent across pathways

Finally, we investigated whether inter-mosaic coordination was present between types of RGC that encode distinct visual features (for example, ON brisk transient and OFF brisk sustained or ON brisk transient and ON brisk sustained). Mosaic pairs that differed in their feature selectivity appeared statistically independent (Extended Data Fig. 4a, b, d, f, h;

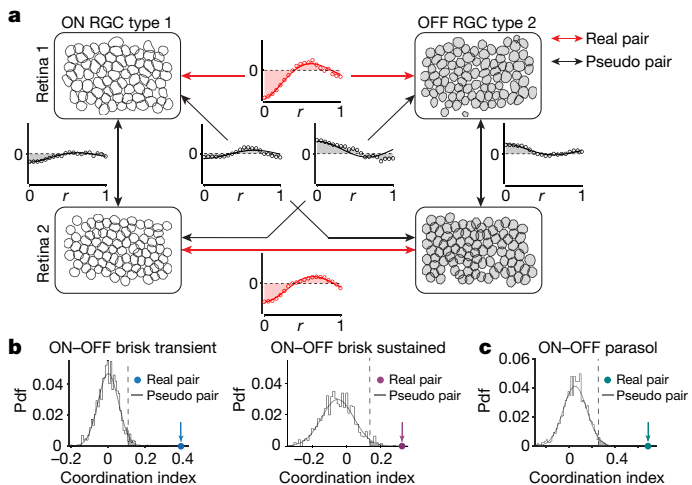


**Fig. 4 | Mosaic anti-alignment is unlikely to have arisen by chance.**

**a**, Example mosaics of ON (left) and OFF (right) parasol RGCs from two retinas. Red arrows, mosaics from the same retina (real pairs); black arrows, mosaics from different retinas (pseudo-pairs). Insets, radial average z-scored IMCE (open circles) for real (red) and pseudo (grey) mosaic pairs. Parametric fit (solid line) and area under curve (shaded region) are used to estimate coordination index (see Methods). x-axis shows normalized radial shift  $r$ . **b**, Sampling distribution from bootstrap estimates of mean coordination index for pseudo pairs (grey) and real pairs (filled coloured circles) for ON-OFF brisk transient and ON-OFF brisk sustained rat RGCs. Pdf, probability density function. Number of real, pseudo pairs: 5, 40 (left); 3, 12 (right). Coordination index (mean  $\pm$  s.d.):  $0.39 \pm 0.13$  (left);  $0.33 \pm 0.19$  (right). Grey shaded region to right of vertical dashed line indicates value exceeding 95% confidence interval based on one-sample two-sided  $t$ -test statistic. **c**, As in **b** for ON-OFF primate parasol mosaics. Number of real, pseudo pairs: 3, 12. Coordination index,  $0.68 \pm 0.13$ .  $P$  and Cohen's  $d$  are:  $3.03 \times 10^{-8}$  and  $1.61$ ,  $3.72 \times 10^{-3}$  and  $1.23$ , and  $8.78 \times 10^{-48}$  and  $1.19$ , for ON-OFF brisk transient, ON-OFF brisk sustained, and ON-OFF parasol, respectively. Results are representative of  $n = 5$  retinas for ON-OFF brisk transient,  $n = 3$  retinas for ON-OFF brisk sustained, and  $n = 3$  retinas for ON-OFF parasol RGC types.

Extended Data Table 2), because the coordination index of these pairs did not fall outside the null distribution established from pseudo-pairs (Extended Data Fig. 4c, e, g, i). Thus, mosaic anti-alignment seems to be restricted to pairs of RGC types that form pathways that encode similar visual features with ON and OFF responses.

## Discussion

We have shown that ECT predicts, and measurements confirm, that ON and OFF mosaics with similar feature selectivity are anti-aligned to optimize the encoding of natural scenes (Figs. 1, 3, 4). This indicates that instead of each type of RGC representing an independent and parallel pathway of visual signalling, at least some pairs of RGC types have spatially coordinated RF mosaics, and this coordination is likely to support the efficient encoding of natural scenes.

We speculate that anti-alignment is preferred because it mitigates the effects of noise. When input and output noise in the efficient coding model were small (for example, the variability was less than the mean) the optimized mosaics were aligned. We think that the higher noise state is more likely to be representative of retinal processing because there are many sources of Poisson-like noise in the retina. For example, at the input stage of retinal processing, the absorption of photons follows a Poisson distribution. Within photoreceptors, the spontaneous activation of phototransduction molecules, along with Poisson-like variability in vesicular glutamate release, add substantial amounts of noise<sup>29–32</sup>. After the photoreceptors, noise is further added by bipolar

cells and in spike generation by RGCs<sup>33,34</sup>. The input and output noise in the efficient coding model are not easily mapped onto these biological noise sources. However, retinal noise is substantial and is thought to strongly influence mammalian vision<sup>9,35–37</sup>. Furthermore, noise is likely to dominate signalling under conditions that are most relevant to survival, such as detecting camouflaged predators or prey. Thus, anti-alignment might be a strategy to increase the reliability of coding when noise dominates signal.

To investigate how much anti-aligned mosaics improve the encoding of natural scenes, we compared the mutual information between a test set of natural scenes and two mosaic pairs: one ON-OFF pair that was anti-aligned, and a second pair that was aligned. The aligned pair encoded about 4% less information than the anti-aligned pair (see Methods). For context, elimination of the RF surrounds in two mosaics of anti-aligned ON and OFF RGCs resulted in a decrease of about 19% in mutual information. Thus, inter-mosaic coordination represents about 20% of the encoding benefit provided by RF surrounds, which are broadly considered to be fundamental to early visual processing.

One important caveat to these results is that RF structure can depend on light level and other stimulus variables<sup>38,39</sup>. Thus, anti-alignment could also depend on stimulus conditions. In one experiment, we tested the persistence of anti-alignment from the cone-mediated light levels examined here (Fig. 4) to rod-mediated light levels (Extended Data Fig. 5). The anti-alignment among ON and OFF brisk transient RGCs persisted, but ON and OFF brisk sustained mosaics were insufficiently complete in this experiment for a conclusive test. More experiments are needed that examine a wider range of stimulus manipulations, but these data suggest that mosaic anti-alignment persists across light levels.

The second caveat is that the ECT model used here is optimized on natural scenes, not natural movies. As such, it is tractable, but generates only two ‘cell types’: an ON and an OFF type. However, the mammalian retina contains many RGC types that can encode distinct features (for example, direction selectivity versus chromatic selectivity). Whether there exists any coordination between these RGC mosaics has yet to be determined, but it motivates further studies of optimizing a model retina on natural movies with chromatic content. This optimization may need to include head and eye movements, with global and local motion to mimic animals moving through natural environments.

The anti-alignment of ON and OFF mosaics could support aspects of visual processing beyond efficient coding, such as the formation of orientation tuning in V1<sup>11,40</sup>. A V1 neuron could receive input (indirectly) from two randomly selected nearby ON and OFF RGCs and form an orientation-tuned RF if the mosaics were anti-aligned.

Finally, these results raise questions about the developmental and synaptic mechanisms that produce inter-mosaic coordination—for example, whether this coordination requires visual experience or is genetically programmed. While these questions await further investigation, our results show that distinct cell types can exhibit precise and highly specific spatial coordination within a neural circuit, conferring advantages for the efficient encoding of natural stimuli.

## Online content

Any methods, additional references, Nature Research reporting summaries, source data, extended data, supplementary information, acknowledgements, peer review information; details of author contributions and competing interests; and statements of data and code availability are available at <https://doi.org/10.1038/s41586-021-03317-5>.

1. Devries, S. H. & Baylor, D. A. Mosaic arrangement of ganglion cell receptive fields in rabbit retina. *J. Neurophysiol.* **78**, 2048–2060 (1997).
2. Field, G. D. & Chichilnisky, E. J. Information processing in the primate retina: circuitry and coding. *Annu. Rev. Neurosci.* **30**, 1–30 (2007).
3. Wässle, H., Peichl, L. & Boycott, B. B. Dendritic territories of cat retinal ganglion cells. *Nature* **292**, 344–345 (1981).
4. Wässle, H., Peichl, L. & Boycott, B. B. Morphology and topography of on- and off-alpha cells in the cat retina. *Proc. R. Soc. Lond. B Biol. Sci.* **212**, 157–175 (1981).

5. Callaway, E. M. Structure and function of parallel pathways in the primate early visual system. *J. Physiol. (Lond.)* **566**, 13–19 (2005).
6. Karklin, Y. & Simoncelli, E. P. Efficient coding of natural images with a population of noisy linear–nonlinear neurons. *Adv. Neural Inf. Process. Syst.* **24**, 999–1007 (2011).
7. Bae, J. A. et al. Digital museum of retinal ganglion cells with dense anatomy and physiology. *Cell* **173**, 1293–1306.e19 (2018).
8. Borghuis, B. G., Ratliff, C. P., Smith, R. G., Sterling, P. & Balasubramanian, V. Design of a neuronal array. *J. Neurosci.* **28**, 3178–3189 (2008).
9. Gjorgjieva, J., Sompolsky, H. & Meister, M. Benefits of pathway splitting in sensory coding. *J. Neurosci.* **34**, 12127–12144 (2014).
10. Ratliff, C. P., Borghuis, B. G., Kao, Y. H., Sterling, P. & Balasubramanian, V. Retina is structured to process an excess of darkness in natural scenes. *Proc. Natl Acad. Sci. USA* **107**, 17368–17373 (2010).
11. Jang, J. & Paik, S. B. Interlayer repulsion of retinal ganglion cell mosaics regulates spatial organization of functional maps in the visual cortex. *J. Neurosci.* **37**, 12141–12152 (2017).
12. Kremkow, J., Jin, J., Wang, Y. & Alonso, J. M. Principles underlying sensory map topography in primary visual cortex. *Nature* **533**, 52–57 (2016).
13. Lee, K. S., Huang, X. & Fitzpatrick, D. Topology of ON and OFF inputs in visual cortex enables an invariant columnar architecture. *Nature* **533**, 90–94 (2016).
14. Mazade, R., Jin, J., Pons, C. & Alonso, J. M. Functional specialization of ON and OFF cortical pathways for global-slow and local-fast vision. *Cell Rep.* **27**, 2881–2894.e5 (2019).
15. Rockhill, R. L., Euler, T. & Masland, R. H. Spatial order within but not between types of retinal neurons. *Proc. Natl Acad. Sci. USA* **97**, 2303–2307 (2000).
16. Wässle, H., Boycott, B. B. & Illing, R. B. Morphology and mosaic of on- and off-beta cells in the cat retina and some functional considerations. *Proc. R. Soc. Lond. B Biol. Sci.* **212**, 177–195 (1981).
17. Brown, S. P., He, S. & Masland, R. H. Receptive field microstructure and dendritic geometry of retinal ganglion cells. *Neuron* **27**, 371–383 (2000).
18. Doi, E. et al. Efficient coding of spatial information in the primate retina. *J. Neurosci.* **32**, 16256–16264 (2012).
19. Galli-Resta, L., Novelli, E., Kryger, Z., Jacobs, G. H. & Reese, B. E. Modelling the mosaic organization of rod and cone photoreceptors with a minimal-spacing rule. *Eur. J. Neurosci.* **11**, 1461–1469 (1999).
20. Eglen, S. J., Diggle, P. J. & Troy, J. B. Homotypic constraints dominate positioning of on- and off-center beta retinal ganglion cells. *Vis. Neurosci.* **22**, 859–871 (2005).
21. Eglen, S. J. Development of regular cellular spacing in the retina: theoretical models. *Math. Med. Biol.* **23**, 79–99 (2006).
22. Dabrowski, W., Grybos, P. & Litke, A. M. A low noise multichannel integrated circuit for recording neuronal signals using microelectrode arrays. *Biosens. Bioelectron.* **19**, 749–761 (2004).
23. Ravi, S., Ahn, D., Greschner, M., Chichilnisky, E. J. & Field, G. D. Pathway-specific asymmetries between ON and OFF visual signals. *J. Neurosci.* **38**, 9728–9740 (2018).
24. Chichilnisky, E. J. A simple white noise analysis of neuronal light responses. *Network* **12**, 199–213 (2001).
25. Yu, W. Q., Grzywacz, N. M., Lee, E. J. & Field, G. D. Cell type-specific changes in retinal ganglion cell function induced by rod death and cone reorganization in rats. *J. Neurophysiol.* **118**, 434–454 (2017).
26. Anishchenko, A. et al. Receptive field mosaics of retinal ganglion cells are established without visual experience. *J. Neurophysiol.* **103**, 1856–1864 (2010).
27. Gauthier, J. L. et al. Uniform signal redundancy of parasol and midget ganglion cells in primate retina. *J. Neurosci.* **29**, 4675–4680 (2009).
28. Watanabe, M. & Rodieck, R. W. Parasol and midget ganglion cells of the primate retina. *J. Comp. Neurol.* **289**, 434–454 (1989).
29. Angueyra, J. M. & Rieke, F. Origin and effect of phototransduction noise in primate cone photoreceptors. *Nat. Neurosci.* **16**, 1692–1700 (2013).
30. Donner, K. Noise and the absolute thresholds of cone and rod vision. *Vision Res.* **32**, 853–866 (1992).
31. Dunn, F. A. & Rieke, F. The impact of photoreceptor noise on retinal gain controls. *Curr. Opin. Neurobiol.* **16**, 363–370 (2006).
32. Rao-Miroznikoff, R., Buchsbaum, G. & Sterling, P. Transmitter concentration at a three-dimensional synapse. *J. Neurophysiol.* **80**, 3163–3172 (1998).
33. Berry, M. J., Warland, D. K. & Meister, M. The structure and precision of retinal spike trains. *Proc. Natl Acad. Sci. USA* **94**, 5411–5416 (1997).
34. Freed, M. A. & Liang, Z. Synaptic noise is an information bottleneck in the inner retina during dynamic visual stimulation. *J. Physiol. (Lond.)* **592**, 635–651 (2014).
35. Atick, J. J. & Redlich, A. N. What does the retina know about natural scenes? *Neural Comput.* **4**, 196–210 (1992).
36. Brinkman, B. A., Weber, A. I., Rieke, F. & Shea-Brown, E. How do efficient coding strategies depend on origins of noise in neural circuits? *PLoS Comput. Biol.* **12**, e1005150 (2016).
37. Field, G. D. & Sampath, A. P. Behavioural and physiological limits to vision in mammals. *Phil. Trans. R. Soc. Lond. B* **372**, 20160072 (2017).
38. Barlow, H. B., Fitzhugh, R. & Kuffler, S. W. Change of organization in the receptive fields of the cat's retina during dark adaptation. *J. Physiol. (Lond.)* **137**, 338–354 (1957).
39. Hosoya, T., Baccus, S. A. & Meister, M. Dynamic predictive coding by the retina. *Nature* **436**, 71–77 (2005).
40. Ringach, D. L. On the origin of the functional architecture of the cortex. *PLoS ONE* **2**, e251 (2007).

**Publisher's note** Springer Nature remains neutral with regard to jurisdictional claims in published maps and institutional affiliations.

© The Author(s), under exclusive licence to Springer Nature Limited 2021

## Methods

### Animals and recording

All procedures involving the use of animals were approved by the Institutional Animal Care and Use Committee. Macaque monkeys (*Macaca mulatta*) and Long-Evans (LE) rats were used in these experiments. Preparation of primate retinas followed previously described protocols<sup>41,42</sup>, and primate data were generously provided by E.J. Chichilnisky. For experiments with rat retinas, animals between the ages of 3 months and 1 year were used. Both male and female primates and rats were included. Animals were housed under a 12-h light–dark cycle with ad lib access to food and water. Rats were dark adapted for 12–16 h before the experiment. Rats were deeply anaesthetized by intraperitoneal injection of ketamine (0.1 mg/10 mg body weight) and xylazine (0.1 mg/20 mg body weight), anaesthesia was confirmed by extinguished eyeblink and toe-pinch reflexes, and rats were killed by decapitation. The eyes were immediately enucleated and placed in a Petri dish filled with bicarbonate buffered Ames medium (Sigma, St. Louis, MO) bubbled with 5% oxygen and 95% carbon dioxide maintained at 35–36 °C with pH 7.4. Following hemi-section and vitrectomy, the retina was detached from the sclera and a small piece (~1.5 mm × 3 mm) was cut from the medial-dorsal region and placed on a multielectrode array (512 electrodes, 60 µm pitch), RGC-side down. Euthanasia and retinal dissections were performed in a completely dark room with the assistance of infrared lamps and infrared converting goggles.

Spikes on the MEA were identified by previously described methods<sup>23,43</sup>. In brief, extracellular voltages were sampled at 20 kHz and stored for offline analysis. Spikes were dually sorted using a JAVA-based custom automated algorithm and YASS<sup>44,45</sup>, principal component analysis (PCA) was used to reduce the dimensionality of the data, and a mixture of Gaussians model was fit to extract clusters of spikes. Errors in spike clustering were corrected by manually adjusting the location and number of Gaussians fit to the data<sup>46</sup>. Each spike cluster was assigned to a putative RGC if the ensemble of spikes exhibited a refractory period of at least 1.5 ms with <10% estimated contamination and at least 100 spikes. Individual RGCs were tracked across multiple stimulus conditions by checking for correspondence in clustered spike shapes and the electrophysiological image<sup>47,48</sup>.

### Visual stimuli and classification of RGCs into distinct functional types

A gamma-corrected OLED display (SVGA+3XL, Emagin Corporation) refreshing at 60.35 Hz was used to display visual stimuli to the retina. The stimuli were focused on the photoreceptor outer segments using an inverted microscope (Nikon Eclipse TE-2000U). The mean intensity of the visual stimulus at the photoreceptors was ~7,000 photoisomerizations per M-cone per s for rat retinas, and ~1,700 photoisomerizations per M-cone per s for monkey retinas, at photopic light level. At scotopic light level, the intensity values were ~1.7 photoisomerizations per rod per s for these retinas.

RGCs were classified into distinct types using previously described methods<sup>23,24</sup>. We used binary checkerboard noise, with ~40 µm × 40 µm checkers for rat retinas and ~55 µm × 55 µm checkers for monkey retinas. The images refreshed every one or two frames. We computed the spike-triggered average (STA) stimulus as an estimate of the spatiotemporal RFs of individual RGCs<sup>24</sup>. In conjunction, response properties such as spike rate, autocorrelation and contrast selectivity were used to serially classify RGCs into different groups. The union of RFs obtained from the automated spike sorting algorithm and YASS<sup>44,45</sup> was taken to generate the complete RF mosaic for each group of classified RGCs. Identification of irreducible RGC types was confirmed by observing a mosaic-like arrangement of spatial RFs.

### Estimating RF locations and plotting mosaics

The spatial RFs of individual RGCs were extracted as follows: stimulus pixels (checkers) across frames of the STA that exceed 4 s.d. above or

below the mean intensity across all stimulus pixels were selected. The average time course of pixel intensity values of the selected pixels was computed as an estimate of the temporal RF. The inner product of the temporal RF and each pixel of the STA across time was computed, which collapsed the spatiotemporal STA to a single frame; pixels that evolved in time in a manner similar to the temporal RF had high values and those that did not had small values. This single frame was taken as an estimate of the spatial RF<sup>41</sup>. This procedure assumes that the spatiotemporal RF is the outer product of two filters: a spatial and a temporal filter. Singular value decomposition performed on the full spatiotemporal RF yielded similar results. Specifically, the first vector pair (those with the highest associated singular value) yielded an estimate of the temporal and spatial RFs that closely matched the procedure described above, but in general exhibited greater noise<sup>23</sup>.

After obtaining the spatial RF, stimulus pixels exceeding 5% of the peak pixel were identified and used to calculate the COM of the spatial RF. To plot RF mosaics, the spatial RF was filtered by a Gaussian function with a standard deviation of 0.75 pixels (1.5 pixels for ON brisk sustained cells), and a contour at 61% (-1 s.d. for a Gaussian RF) of the peak pixel was extracted using the contour function in MATLAB (Mathworks).

### Analysis of mosaic coordination

To analyse RF coordination between mosaics of distinct RGC types, we computed an inter-mosaic coordination energy (IMCE). We call it an ‘energy’ because it is analogous to postulating a repulsive ‘force’ between heterotypic cell types and integrating these forces to calculate an energy of the system. To compute IMCE, each spatial RF was summarized by a single point at the COM of the RF. Then, the relative spatial distances between the RF COMs across the two mosaics were assessed by computing the inverse of the squared distances between all heterotypic points (Fig. 2d). Specifically, for a pair of points  $i$  and  $j$  separated by a distance  $r_{ij}$ , their contribution is:

$$E_{ij} = \frac{1}{r_{ij}^2} \quad (1)$$

To prevent  $E_{ij}$  from diverging as two points come very close to one another,  $E_{ij}$  is set to a constant value if the distance between points is smaller than a threshold value set by  $r_{\min}$ :

$$E_{ij} = \frac{1}{(r_{ij} - r_{\min})^2} \text{ for } r_{ij} > r_{\min} \quad (2)$$

$$E_{ij} = \frac{1}{r_{\min}^2} \text{ for } r_{ij} \leq r_{\min} \quad (3)$$

The value for  $r_{\min}$  was set to 0.20 times the median nearest-neighbour distance between heterotypic points<sup>4</sup> (see also Fig. 2d). Qualitative results did not depend strongly on the choice of this minimum distance. The values of  $E_{ij}$  were then summed over all heterotypic pairs and divided by the total number of pairs to obtain:

$$E_m = \frac{1}{N} \sum_{i \neq j}^N E_{ij} \quad (4)$$

which provides a metric summarizing pairwise spacing between RF COMs, emphasizing nearby pairs and de-emphasizing distant pairs.

The next step of the analysis was to compare the observed  $E_m$  to that for other possible nearby arrangements of the two mosaics, while keeping the intra-mosaic arrangement fixed. To achieve this, all points from one mosaic were rigidly translated while keeping the other mosaic fixed and recomputing  $E_m$ . This process was repeated for different amounts of shift in different directions (Fig. 2e), yielding a 2D matrix given by

$$E_m(\Delta x, \Delta y) = \frac{1}{N} \sum_{i \neq j}^N E_{ij}(\Delta x, \Delta y) \quad (5)$$

This 2D matrix was z-scored to normalize the values to their standard deviation and shifts were normalized to the median homotypic nearest neighbour distance of points from the mosaic kept fixed, to generate a 2D map of IMCE values (Fig. 2f–h):

$$E_{\text{IMC}}(\Delta x, \Delta y) = \frac{E_m(\Delta x, \Delta y) - \langle E_m(\Delta x, \Delta y) \rangle}{\sigma_{E_m(\Delta x, \Delta y)}} \quad (6)$$

Radially averaging the IMCE map yields a curve that summarizes the spatial relationship between mosaics. If mosaics are aligned, then RFs are close to one another and the IMCE is high at zero shift and tends to fall when one mosaic is shifted with respect to the other mosaic (Fig. 2b, g, j). However, if mosaics are anti-aligned, then RFs are far from one another and the IMCE is relatively low at zero shift and tends to rise as one mosaic is shifted with respect to the other mosaic (Fig. 2a, f, i). To investigate the presence of higher-order structures in the 2D IMCE maps, we analysed the power spectrum and singular value decomposition of 2D IMCE maps from multiple retinas. A concentration of power mainly at low frequencies and a low rank decomposition of the 2D IMCE maps indicated that radial average captures the most dominant feature associated with mosaic coordination. However, absence of higher order structure may reflect limitations in our data (for example, the number of RGCs sampled over the MEA).

### Definition and controls for ROI choice

The lattices formed by the RF COMs are finite and relatively small—limited by the recording area of the MEA and the size of RFs. As a result, the continuity of RF arrangement breaks down near the edge of the measured mosaic. To mitigate potential bias in the estimated IMCE introduced by this discontinuity, we defined an ROI—a geometric area within which the density of RFs is approximately homogeneous for both mosaics and whose edges are at least 1.2 median homotypic nearest-neighbour distance from the boundary (Fig. 3c, f). For a relatively periodic arrangement of RFs, a shift of one median inter-cell distance would be approximately equal to one spatial period, which when applied to one set of points, would move them such that they would occupy the positions of their nearest neighbours in the direction of the shift. Shifts limited to <1.2 median homotypic nearest-neighbour distance within an ROI with spatially homogenous density of points, would (on average) preserve the spatial density of points inside the ROI for each shift, thus mitigating bias from discontinuity and variations in spatial density of points at the boundary. For a continuous lattice, exemplified by hexagonal lattices with spatial noise (Fig. 2a, b), the ROI can be a circle or any polygon whose boundary lies at least one median inter-cell distance inside the lattice boundary. We tested rectangular, convex hull and non-convex hull ROIs with boundaries that fell within 1.2 median inter-cell distances of the mosaic borders, and shift distances restricted to one median inter-cell distance. The results did not qualitatively depend on the choice of ROI shape.

### Simulating ON and OFF mosaic coordination using a modified PIPP model

We used a modified PIPP model to generate pairs of mosaics with specific types of coordination<sup>21,49</sup>. We first generated a mosaic consisting of  $N$  points by adding points sequentially to a 2D plane such that each new point lies outside a jittered radius centred around all the other existing points. Thus, the probability of adding a new point  $i$  of type 1 at location  $\vec{r}_{1i}$  is:

$$P_{1i} = \max\left(0, \prod_j \operatorname{sgn}\left(\left|\vec{r}_{1i} - \vec{r}_{1j \neq i}\right| - d_{\text{exc}}\right)\right) \quad (7)$$

where the homotypic exclusion distance  $d_{\text{exc}} = d_{\min} + \zeta$ . The minimum distance  $d_{\min}$  is set by the areal density of points, such that no two points can lie closer than  $2d_{\min}$ . The value of the jitter parameter  $\zeta$  is obtained from an independent draw from normal distribution with mean zero and standard deviation  $0.12 \times d_{\min}$ . This process is repeated until all  $N$  points are added to the plane.

To generate a second mosaic that is anti-aligned with the first (Fig. 2a), new points of type 2 are added to the same plane such that each new point  $i$  satisfies the homotypic exclusion rule defined by equation (7) and the heterotypic exclusion rule:

$$P_{2i} = \max\left(0, \prod_j \operatorname{sgn}\left(\left|\vec{r}_{1i} - \vec{r}_{2j \neq i}\right| - d_{\text{exc}}\right)\right) \quad (8)$$

where the heterotypic exclusion distance  $d'_{\text{exc}} = d_{\min} + \zeta'$ . The values of  $d_{\min}$  and  $\zeta'$  are set by the mean nearest-neighbour distance of homotypic points of the first mosaic and a draw from normal distribution with mean zero and standard deviation  $0.60 \times d_{\min}$ . To generate a second mosaic that is aligned with the first, (Fig. 2b) the heterotypic exclusion rule is modified to:

$$P_{2i} = \max\left(0, \prod_j \operatorname{sgn}\left(d_{\text{exc}} - \left|\vec{r}_{1i} - \vec{r}_{2j \neq i}\right|\right)\right) \quad (9)$$

where the values of  $d_{\min}$  and  $\zeta'$  are set by the mean nearest-neighbour distance of homotypic points of the first mosaic and a draw from normal distribution with mean zero and standard deviation  $0.35 \times d_{\min}$ . To generate a second mosaic that is independent of the first, new points are added obeying only the homotypic exclusion rule (equation (7)).

### Significance testing for inter-mosaic coordination

To determine whether the radial IMCE for the measured ON and OFF mosaic pairs are statistically distinct from those of independent mosaics, we used a permutation test by combining mosaics measured from different retinas. Two mosaics from different retinas (and hence different experiments), which we call ‘pseudo-pairs’, ought to exhibit no coordination, that is, they are statistically independent on average. To estimate the IMCE for these pseudo-pairs of mosaics, we first spatially registered each mosaic pair. This was achieved by computing the COM of all the individual RF centres for each mosaic and then aligning the two COMs such that the two mosaics occupy the same region of space. Next, we generated a null distribution of radial IMCE for these pseudo mosaic pairs (Fig. 4a). The radial IMCE curves were further distilled to a single number we term the coordination index (CI) by first estimating the absolute value of the area under the curves. These areas were computed by first fitting the radial IMCE with a damped cosine function:

$$E_{\text{Rad}}(r) = a \times \cos(r + \phi) \times e^{-b \times r/c} + d \quad (10)$$

where  $a \geq 0$ ,  $\phi$ ,  $b$ ,  $c$  and  $d$  are fitting parameters. The damped cosine function fit well the radial IMCE curves of both real and pseudo mosaic pairs, thereby providing an accurate estimate of the area under these curves (Fig. 4a). These areas were then converted into CIs by assigning the areas a positive value if the value of  $E_{\text{Rad}}(r=0) \leq 0$ , and a negative value if  $E_{\text{Rad}}(r=0) > 0$ . This caused radial IMCEs such as those in Fig. 2i, j to have relatively large positive and negative CIs, respectively. The CIs for radial IMCEs like that in Fig. 2k were near zero.

For a given set of real mosaic pairs (for example, ON and OFF brisk transient RGCs), the average of their CIs was computed. We then compared this average CI value to the distribution of bootstrapped averages over an equivalent number of samples from the distribution of CIs generated from pseudo mosaic pairs (Fig. 4b). Note, the distributions in Fig. 4 are mean CI values over these equivalent samples from the ensemble of CI values derived from pseudo-pairs. For example, if there were three real mosaic pairs, three samples were drawn from the

# Article

CIs computed from pseudo mosaic pairs and these were averaged to generate an expected value from sampling three independent (pseudo) mosaic pairs. This process was repeated 1,000 times ( $n=1,000$  bootstrap samples) to generate a null distribution of average CIs to which the observed CI was compared (for example, Fig. 4b, c). If the observed CI lay outside the 95% confidence interval of the null distribution, the observed coordination was considered statistically significant.

## Efficient coding model

The efficient coding model is an extension of previous work on the optimal coding of natural scenes<sup>6</sup>. Patches of natural scenes<sup>50</sup>, each  $18 \times 18 = 324$  pixels in size, are provided as inputs to the model. To reduce edge effects, we multiply each input image by a circular mask of a 9-pixel radius, which effectively leaves about 254 pixels in each input image patch. The patches are filtered by an array of linear filters, each corresponding to a model neuron. The total number of model neurons is kept fixed during training. For each model neuron, the output of the linear filter  $y_j$  is passed through a softplus nonlinearity  $f_j$ :

$$f_j(y_j) = \log(1 + \exp(\beta \times y_j)) / \beta \quad (11)$$

to obtain the response  $r_j$  (Fig. 1a) with independently learnable parameters for threshold and slope in the softplus function:

$$r_j(y_j) = a \times f_j(y_j - b) \quad (12)$$

The response  $r$  represents the firing rate of the modelled RGC. For speed in training, the value of  $\beta$  is kept constant at 2.5. Two i.i.d. Gaussian noises with  $\sigma = 0.4$  and  $\sigma = 3.0$  are added to the stimulus and the response, respectively. In addition, we impose metabolic costs for generating spikes by constraining the mean firing rate to be 1 for each neuron. The qualitative results of the optimization did not depend on these parameter choices.

The model is trained using a stochastic gradient method (learning rate of 0.001) to maximize mutual information (MI) between input images and output firing rates. To constrain the mean firing rate, we use the augmented Lagrangian method<sup>51</sup> and reverse the sign of the partial derivatives with respect to the Lagrange multipliers during the gradient descent procedure. Filter weights were initialized as  $18 \times 18$  white noise images (Fig. 1b) and the initial (log) slope and bias parameters of the nonlinearities were sampled from a uniform distribution [0, 1]. A batch of 100 model neurons was trained for 1,000,000 iterations. The filters were constrained to have unit L2 norm, which is achieved by normalizing the filters after each gradient step. To speed up convergence, we apply two perturbations between 200,000 and 500,000 iterations during training, which we call ‘jittering’ and ‘centring’. The jittering operation is applied every 5,000 iterations, where the filter weights are raised to the power of 1.25; this makes high-amplitude weights of the filters more pronounced while attenuating the low-amplitude weights. The centring operation penalizes the spatial spread of the filters, by adding the mean of the spatial variance of each filter as an additional loss term; this encourages the filter weights to be concentrated around the RF centre. Thus, these perturbations can be conceived as a form of simulated annealing applied periodically to allow RFs to orient relative to one another. The eventual shape of the filters, their organization into mosaics, and the anti-alignment between ON and OFF mosaics did not depend on these jittering and centring procedures<sup>6</sup>, but they speeded up the convergence of the model.

To quantify the impact of mosaic coordination on the information encoded about natural scenes (see Discussion), we compared the MI that a pair of anti-aligned mosaics conveyed about natural scenes with

that of a pair of aligned mosaics. The anti-aligned ON–OFF mosaics were obtained from the efficient coding model. The aligned mosaics were generated by first taking the RF centres of the ON mosaic from the anti-aligned mosaic pair and then duplicating these with a polarity flip to generate the OFF mosaic, such that the ON and OFF units were aligned. The centre–surround structure of the RFs was described as a difference of two Gaussians with different standard deviations but with the same mean defined by the RF centre. To examine the effect of eliminating the RF surrounds, the surround weights were set in the trained model to zero and the RF centres were unaltered. The mutual information between input images and firing rates of model neurons with these centre-only RFs was then compared to that from RFs with the original centre–surround structure to assess the degree to which the RF surround improves natural scene encoding<sup>6</sup>.

## Reporting summary

Further information on research design is available in the Nature Research Reporting Summary linked to this paper.

## Data availability

Raw data will be made available upon request. Source data are provided with this paper.

## Code availability

Analysis code is available at <https://doi.org/10.5281/zenodo.4441277>.

41. Chichilnisky, E. J. & Kalmar, R. S. Functional asymmetries in ON and OFF ganglion cells of primate retina. *J. Neurosci.* **22**, 2737–2747 (2002).
42. Field, G. D. et al. Spatial properties and functional organization of small bistratified ganglion cells in primate retina. *J. Neurosci.* **27**, 13261–13272 (2007).
43. Litke, A. et al. What does the eye tell the brain?: Development of a system for the large-scale recording of retinal output activity. *IEEE Trans. Nucl. Sci.* **51**, 1434–1440 (2004).
44. Lee, J. H. et al. in *Advances in Neural Information Processing Systems* (eds. Guyon, I. et al.) 4002–4012 (Curran Associates, 2017).
45. Lee, J. et al. YASS: yet another spike sorter applied to large-scale multi-electrode array recordings in primate retina. Preprint at *bioRxiv* <https://doi.org/10.1101/2020.03.18.997924> (2020).
46. Shlens, J. et al. The structure of multi-neuron firing patterns in primate retina. *J. Neurosci.* **26**, 8254–8266 (2006).
47. Gauthier, J. L. et al. Receptive fields in primate retina are coordinated to sample visual space more uniformly. *PLoS Biol.* **7**, e1000063 (2009).
48. Yao, X. et al. Gap junctions contribute to differential light adaptation across direction-selective retinal ganglion cells. *Neuron* **100**, 216–228.e6 (2018).
49. Eglen, S. J. The role of retinal waves and synaptic normalization in retinogeniculate development. *Phil. Trans. R. Soc. Lond. B* **354**, 497–506 (1999).
50. Doi, E., Inui, T., Lee, T. W., Wachtler, T. & Sejnowski, T. J. Spatiochromatic receptive field properties derived from information-theoretic analyses of cone mosaic responses to natural scenes. *Neural Comput.* **15**, 397–417 (2003).
51. Nocedal, J. & Wright, S. *Numerical Optimization* (Springer, 2006).

**Acknowledgements** We thank L. Glickfeld, S. Lisberger, F. Rieke, J. Kay and F. Wang for comments on drafts of this manuscript, E. J. Chichilnisky and E. Wu for discussions, E. J. Chichilnisky for primate data, and K. Ruda for assistance with experiments. This work was supported by the Ruth K. Broad Postdoctoral Fellowship (S.R.), the Whitehead Scholars Program (G.D.F.) and NIH/NEI R01 EY031396 (G.D.F.).

**Author contributions** This study was conceived by S.R. and G.D.F. S.R. and E.L.D. analysed data. The efficient coding model and optimizations were implemented by N.Y.J. and J.P. The paper was written by S.R. and G.D.F. and edited by all authors.

**Competing interests** The authors declare no competing interests.

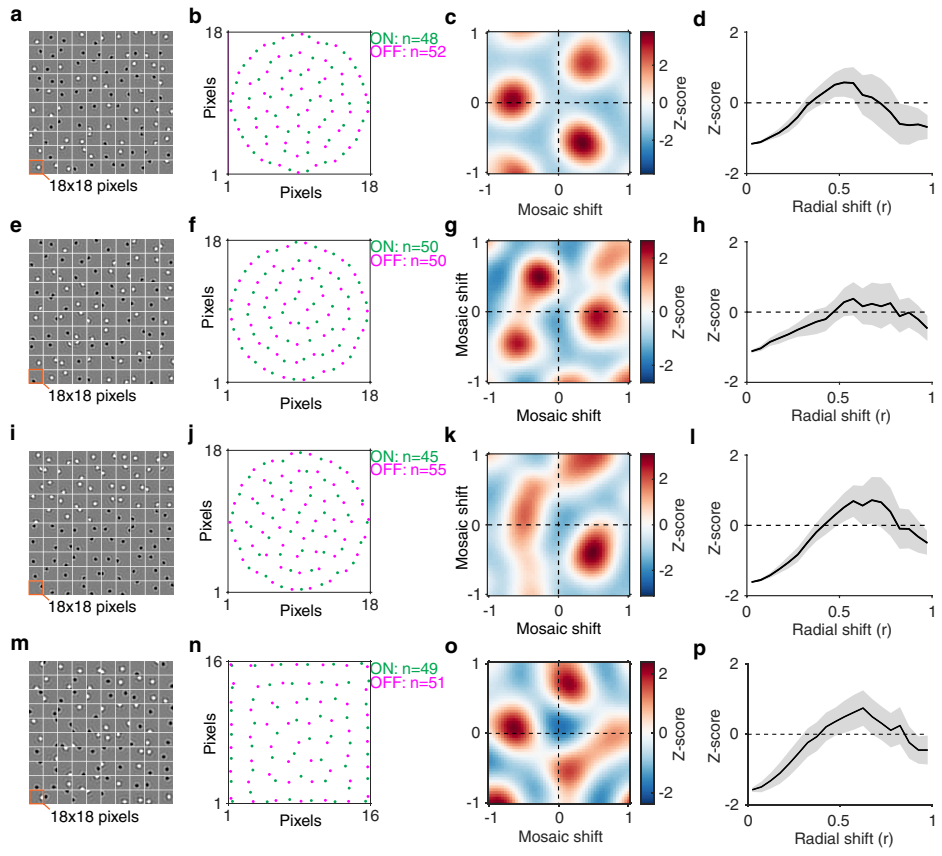
## Additional information

**Supplementary information** The online version contains supplementary material available at <https://doi.org/10.1038/s41586-021-03317-5>.

**Correspondence and requests for materials** should be addressed to G.D.F.

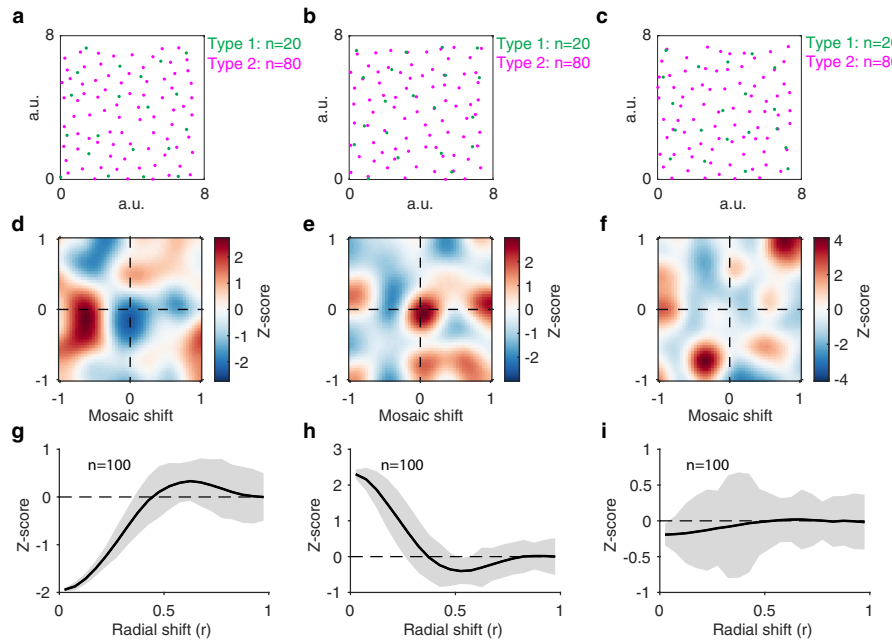
**Peer review information** *Nature* thanks Daniel Kerschensteiner and the other, anonymous, reviewer(s) for their contribution to the peer review of this work.

**Reprints and permissions information** is available at <http://www.nature.com/reprints>.



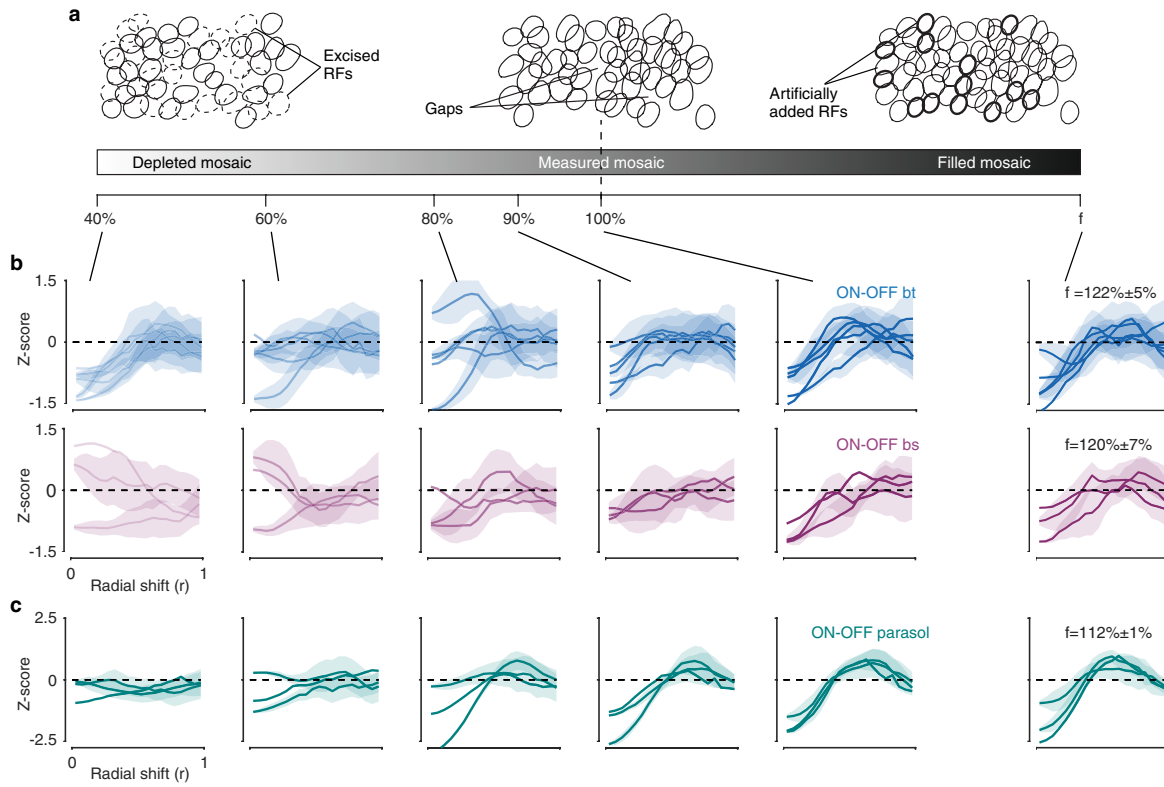
**Extended Data Fig. 1 | Anti-alignment predicted by efficient coding theory is conserved in mosaics with different densities and boundary conditions.** **a**, Optimal spatial filters of 48 ON units and 52 OFF units, each on an  $18 \times 18$ -pixel grid (orange box). **b**, The COMs of optimal filters forming the ON (green) and OFF (magenta) mosaics. Training was performed using a circular mask over the images to reduce edge artefacts. **c, d**, The 2D z-scored IMCE map (**c**) and radial

average z-scored IMCE (**d**) for the mosaic pairs shown in **b, e–h**. As in **a–d** with equal cell density ( $n=50$ ) for ON and OFF mosaics. **i–l**, As in **a–d** with the number of ON and OFF units fixed at  $n=45$  and  $n=55$ , respectively. **m–p**, As in **a–d** with  $n=49$  ON units and  $n=51$  OFF units, but training was performed without a circular mask. Shaded areas, s.d.



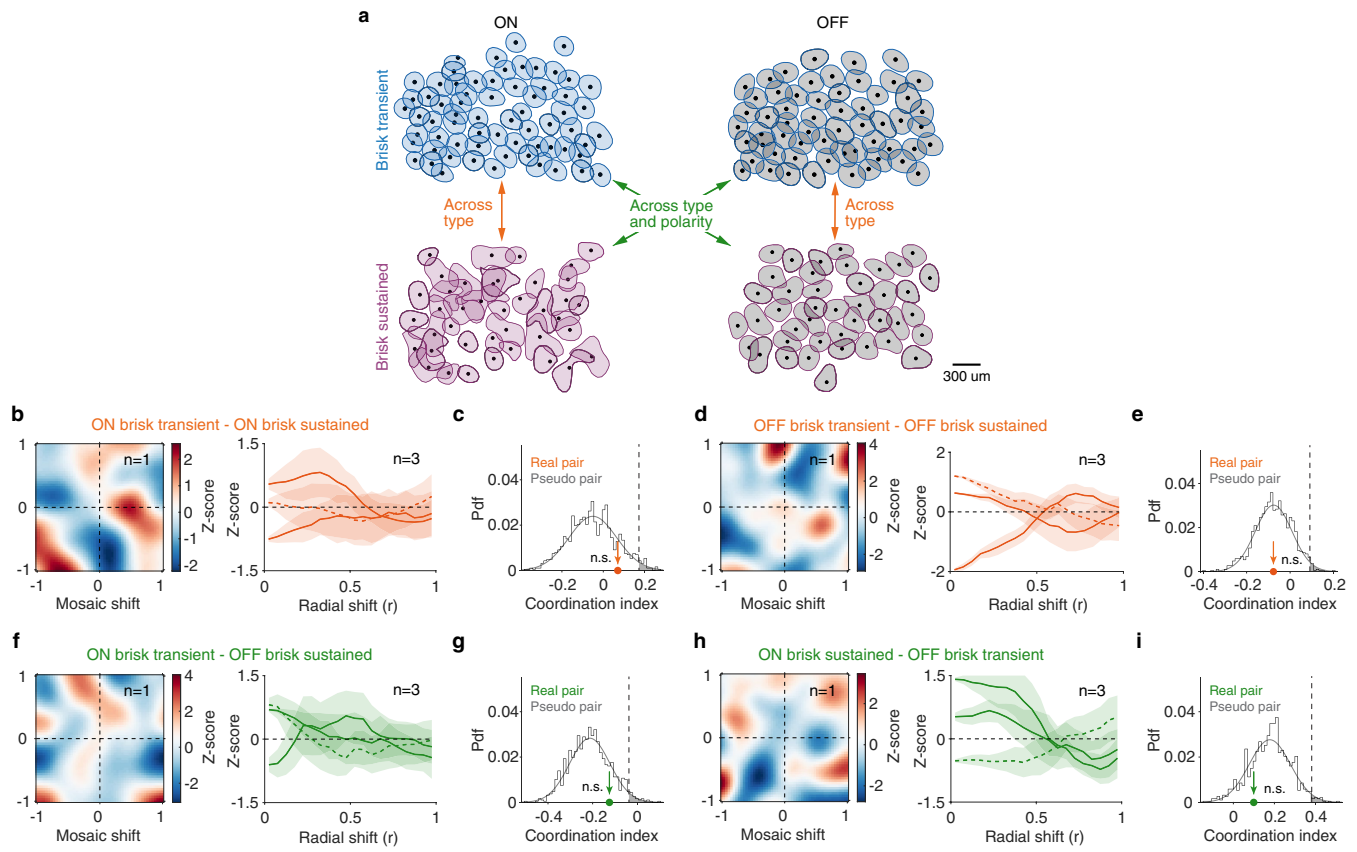
**Extended Data Fig. 2 | Mosaic coordination can persist under widely diverging RF densities.** **a–c**, Bivariate point pattern (type 1: green, type 2: magenta) generated by modified PIPP model (see Methods) with interaction terms for anti-alignment (a), alignment (b) and independence (c). The density

of type 2 points is four times higher than the density of type 1 points. **d–f**, The 2D z-scored IMCE maps corresponding to **a–c**, respectively. **g–i**, The radial average z-scored IMCE averaged over  $n = 100$  mosaic pairs that are aligned (**g**), anti-aligned (**h**) and independent (**i**). Shaded areas are s.e.m.



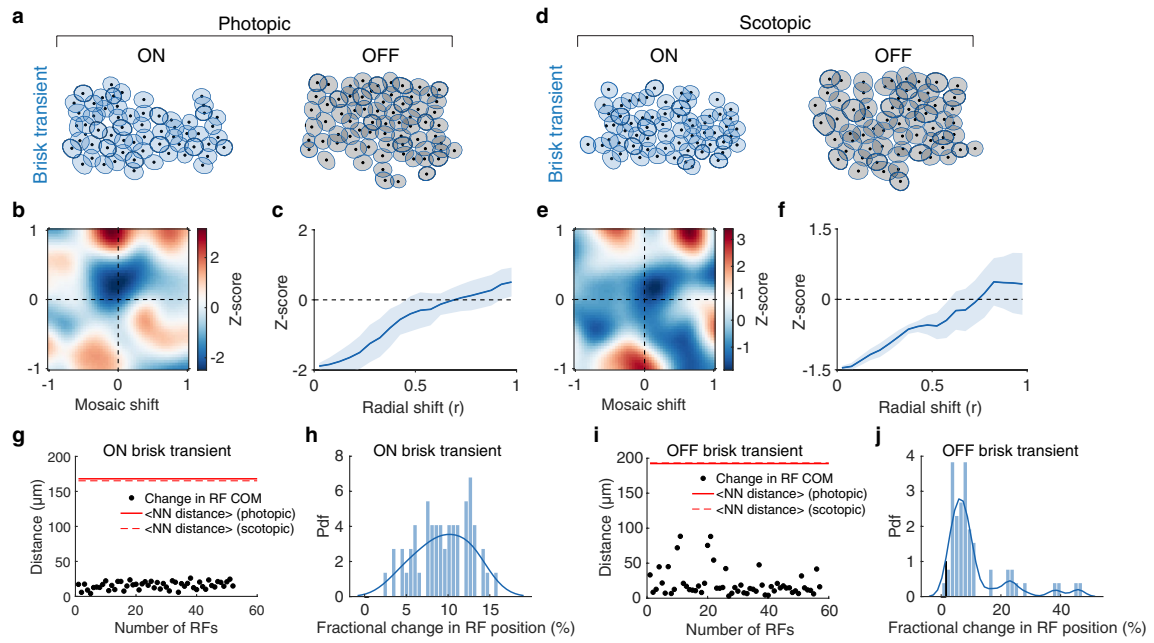
**Extended Data Fig. 3 | Mosaic coordination estimates are robust to RF subsampling.** **a**, RF mosaics illustrating three different cases. Measured, no RFs are removed or added; depleted, a fraction of randomly selected RFs are removed (dashed ellipses); filled, RFs are artificially added to fill mosaic gaps (thick solid ellipses). The gradient below illustrates the percentage of RFs remaining after removing or adding RFs. **b, c**, Radial average z-scored IMCE for different amounts of subsampling and filling of ON and OFF brisk transient

(bt, rat) mosaics (**b**; blue), ON and OFF brisk sustained (**b**; purple), and ON and OFF parasol (primate) mosaics (**c**; green). Each curve corresponds to an individual mosaic pair. Results are representative of  $n=5$  retinas for ON-OFF brisk transient,  $n=3$  retinas for ON-OFF brisk sustained, and  $n=3$  retinas for ON-OFF parasol RGCs. The percentage of RFs relative to measured (100%), is indicated by f. Shaded areas, s.d.



**Extended Data Fig. 4 | Mosaics encoding distinct visual features appear to be independent.** **a**, Example mosaics of ON and OFF brisk transient (bt) and brisk sustained (bs) RGC types. Coordination was tested across cell type (orange), and across cell type and polarity (green). **b, d, f, h**, 2D z-scored IMCE maps of a representative pair (left) and radial average z-scored IMCEs of all pairs (right), for ONbt-ONbs (**b**,  $n=3$ ), OFFbt-OFFbs (**d**,  $n=3$ ), ONbt-OFFbs (**f**,  $n=3$ ), ONbs-OFFbt (**h**,  $n=3$ ) mosaic combinations. Dashed curve, radial average z-scored IMCE corresponding to the 2D z-scored IMCE map (left).

Shaded areas, s.d. **c, e, g, i**, Sampling distributions from bootstrap estimates of mean coordination index for pseudo pairs (grey) and real pairs (orange/green filled circles, arrows). Number of pseudo pairs:  $n=12$  (**c, e, g, i**). The grey shaded region to the right of the vertical dashed line indicates value exceeding 95% confidence interval based on one-sample two-sided  $t$ -test statistic:  $P=0.33$ , 0.98, 0.37 and 0.46, respectively, for **c, e, g** and **i** (n.s., not significant). Cohen's  $d=0.36$ ,  $-0.006$ ,  $0.28$  and  $-0.25$ , respectively, for **c, e, g** and **i**.



**Extended Data Fig. 5 | Anti-alignment between ON brisk transient RF mosaics persists across light levels.** **a**, RF mosaics of ON (left) and OFF (right) brisk transient RGCs, measured at photopic light level (10,000 photo-isomerizations per M-cone per s). The COMs of RFs are indicated by black filled circles. **b**, **c**, 2D z-scored IMCE map (b) and radial average z-scored IMCE (c) for the mosaic pair shown in a. **d**, RF mosaics of ON (left) and OFF (right) brisk transient RGC types, at scotopic light level (1.0 photo-isomerizations per rod per s), from the same retina as in a. **e**, **f**, As in b, c for the mosaic pairs shown in d. **g**, Change in RF

COMs of ON brisk transient RGCs from photopic to scotopic light level (black filled circles). Solid and dashed red lines show homotypic nearest-neighbour (NN) distances between RFs estimated at photopic and scotopic light levels, respectively. **h**, Distribution of fractional change in RF position of ON brisk transient RGCs across light levels expressed as a fraction of the mean NN homotypic distance at photopic light level. Smooth curve, kernel density estimate. **i**, **j**, As in g, h for OFF brisk transient RGCs. Results are representative of  $n=1$  retina. Shaded areas, s.d.

# Article

**Extended Data Table 1 | The distribution of inter-mosaic coordination energy (IMCE) values is approximately normal**

Mosaic pairs	16th percentile	$(\mu - \sigma)\dagger$	84th percentile	$(\mu + \sigma)\dagger$
PIPP* simulated mosaic pairs (Fig. 2a)	0.643	0.638	0.884	0.894
Mosaic pairs from efficient coding model (Fig. 1e)	0.283	0.241	0.685	0.686
Brisk transient mosaic pairs from rat retina (average $\pm$ s.e.m. over 5 retinas: Fig. 3g)	0.025 $\pm$ 0.001	0.025 $\pm$ 0.001	0.033 $\pm$ 0.002	0.034 $\pm$ 0.002
Brisk sustained mosaic pairs from rat retina (average $\pm$ s.e.m. over 3 retinas: Fig. 3i)	0.033 $\pm$ 0.001	0.032 $\pm$ 0.001	0.063 $\pm$ 0.009	0.064 $\pm$ 0.010
Parasol mosaic pairs from primate retina (average $\pm$ s.e.m. over 3 retinas: Fig. 3k)	0.049 $\pm$ 0.001	0.049 $\pm$ 0.002	0.056 $\pm$ 0.002	0.056 $\pm$ 0.002

\*PIPP, pairwise interaction point process.

$\dagger$  $\mu$  and  $\sigma$ , mean and s.d. of IMCE values.

**Extended Data Table 2 | Coordination index values for real and pseudo mosaic pairs**

Species	RGC types *	Coordination	Real pairs ( $\mu \pm \sigma$ )†	Pseudo pairs ( $\mu \pm \sigma$ )†
Rat	ON bt - OFF bt	Anti-aligned	0.393 $\pm$ 0.134	0.002 $\pm$ 0.385
	ON bs - OFF bs		0.326 $\pm$ 0.186	-0.054 $\pm$ 0.360
	ON bt - ON bs	Independent	0.070 $\pm$ 0.437	-0.051 $\pm$ 0.411
	OFF bt - OFF bs		-0.076 $\pm$ 0.715	-0.078 $\pm$ 0.305
	ON bt - OFF bs		-0.124 $\pm$ 0.330	-0.211 $\pm$ 0.324
	ON bs - OFF bt		0.099 $\pm$ 0.360	0.179 $\pm$ 0.366
Primate	ON parasol - OFF parasol	Anti-aligned	0.683 $\pm$ 0.131	0.049 $\pm$ 0.365

\*bt, brisk transient; bs, brisk sustained.

† $\mu$  and  $\sigma$ , mean and s.d. of coordination index.

Corresponding author(s): Greg D Field

Last updated by author(s): 11/17/2020

## Reporting Summary

Nature Research wishes to improve the reproducibility of the work that we publish. This form provides structure for consistency and transparency in reporting. For further information on Nature Research policies, see our [Editorial Policies](#) and the [Editorial Policy Checklist](#).

### Statistics

For all statistical analyses, confirm that the following items are present in the figure legend, table legend, main text, or Methods section.

n/a Confirmed

- The exact sample size ( $n$ ) for each experimental group/condition, given as a discrete number and unit of measurement
- A statement on whether measurements were taken from distinct samples or whether the same sample was measured repeatedly
- The statistical test(s) used AND whether they are one- or two-sided  
*Only common tests should be described solely by name; describe more complex techniques in the Methods section.*
- A description of all covariates tested
- A description of any assumptions or corrections, such as tests of normality and adjustment for multiple comparisons
- A full description of the statistical parameters including central tendency (e.g. means) or other basic estimates (e.g. regression coefficient) AND variation (e.g. standard deviation) or associated estimates of uncertainty (e.g. confidence intervals)
- For null hypothesis testing, the test statistic (e.g.  $F$ ,  $t$ ,  $r$ ) with confidence intervals, effect sizes, degrees of freedom and  $P$  value noted  
*Give P values as exact values whenever suitable.*
- For Bayesian analysis, information on the choice of priors and Markov chain Monte Carlo settings
- For hierarchical and complex designs, identification of the appropriate level for tests and full reporting of outcomes
- Estimates of effect sizes (e.g. Cohen's  $d$ , Pearson's  $r$ ), indicating how they were calculated

*Our web collection on [statistics for biologists](#) contains articles on many of the points above.*

### Software and code

Policy information about [availability of computer code](#)

Data collection

Visual stimuli were displayed using publicly available MGL codebase available at: <http://gru.stanford.edu/doku.php/mgl/overview>. Multielectrode array data were acquired with customized Labview software. The acquisition code will be made available upon reasonable request to the corresponding author.

Data analysis

Spike sorting was performed using a custom Java software and the open source spike sorting algorithm YASS (<https://github.com/paninski-lab/yass>). Data analyses were performed using custom written codes in MATLAB, and will be made available upon request to the corresponding author.

For manuscripts utilizing custom algorithms or software that are central to the research but not yet described in published literature, software must be made available to editors and reviewers. We strongly encourage code deposition in a community repository (e.g. GitHub). See the Nature Research [guidelines for submitting code & software](#) for further information.

### Data

Policy information about [availability of data](#)

All manuscripts must include a [data availability statement](#). This statement should provide the following information, where applicable:

- Accession codes, unique identifiers, or web links for publicly available datasets
- A list of figures that have associated raw data
- A description of any restrictions on data availability

The data that support the findings of this study are available from the corresponding author upon reasonable request.

# Field-specific reporting

Please select the one below that is the best fit for your research. If you are not sure, read the appropriate sections before making your selection.

- Life sciences       Behavioural & social sciences       Ecological, evolutionary & environmental sciences

For a reference copy of the document with all sections, see [nature.com/documents/nr-reporting-summary-flat.pdf](https://nature.com/documents/nr-reporting-summary-flat.pdf)

## Life sciences study design

All studies must disclose on these points even when the disclosure is negative.

Sample size	A minimum of 3 retinas for each retinal ganglion cell type for rat and primate were used for analysis. This sample size satisfied the statistical test of sufficiency for multielectrode array recordings established by previous studies.
Data exclusions	Receptive field mosaics that did not satisfy the minimum number of cells as established through mosaic sub-sampling, were not included in the analysis. This was done to avoid bias in statistical estimates for individual and aggregate data.
Replication	All attempts at replicating experiments and results of statistical tests were successful.
Randomization	All retinas with receptive field mosaics passing the quality control test were included in the analysis with no subsampling, and thus there was no requirement for randomization.
Blinding	Blinding is not relevant to this study because all retinal ganglion cells within each type was included in the analysis without group allocation, and therefore outcomes of statistical tests were not influenced by any group dependent bias.

## Reporting for specific materials, systems and methods

We require information from authors about some types of materials, experimental systems and methods used in many studies. Here, indicate whether each material, system or method listed is relevant to your study. If you are not sure if a list item applies to your research, read the appropriate section before selecting a response.

### Materials & experimental systems

n/a	Involved in the study
<input checked="" type="checkbox"/>	<input type="checkbox"/> Antibodies
<input checked="" type="checkbox"/>	<input type="checkbox"/> Eukaryotic cell lines
<input checked="" type="checkbox"/>	<input type="checkbox"/> Palaeontology and archaeology
<input type="checkbox"/>	<input checked="" type="checkbox"/> Animals and other organisms
<input checked="" type="checkbox"/>	<input type="checkbox"/> Human research participants
<input checked="" type="checkbox"/>	<input type="checkbox"/> Clinical data
<input checked="" type="checkbox"/>	<input type="checkbox"/> Dual use research of concern

### Methods

n/a	Involved in the study
<input checked="" type="checkbox"/>	<input type="checkbox"/> ChIP-seq
<input checked="" type="checkbox"/>	<input type="checkbox"/> Flow cytometry
<input checked="" type="checkbox"/>	<input type="checkbox"/> MRI-based neuroimaging

## Animals and other organisms

Policy information about [studies involving animals](#); [ARRIVE guidelines](#) recommended for reporting animal research

- Laboratory animals      Long-Evans rats, male and female, age 51-215 days. Adult Macaque monkeys, male and female.

- Wild animals      No wild animals were used in this study.

- Field-collected samples      No field-collected samples were used in this study.

- Ethics oversight      Institutional Animal Care and Use Committee at Duke University and at The Salk Institute of Biological Studies.

Note that full information on the approval of the study protocol must also be provided in the manuscript.